This is the accepted version of an article that has been published in
IEEE Transactions on Medical Imaging 29 (11), 1918-1926, 2010 (http://dx.doi.org/10.1109/TMI.2010.2053553) ©IEEE

Factorization Method and Its Physical Justification in Frequency-Difference Electrical Impedance Tomography

Bastian Harrach, Jin Keun Seo, and Eung Je Woo, *Senior Member, IEEE*

***Abstract*—Time-difference electrical impedance tomography (tdEIT) requires two data sets measured at two different times. The difference between them is utilized to produce images of time-dependent changes in a complex conductivity distribution inside the human body. Frequency-difference EIT (fdEIT) was proposed to image frequency-dependent changes of a complex conductivity distribution. It has potential applications in tumor and stroke imaging since it can visualize an anomaly without requiring any time-reference data obtained in the absence of an anomaly. In this paper, we provide a rigorous analysis for the detectability of an anomaly based on a constructive and quantitative physical correlation between a measured fdEIT data set and an anomaly. From this, we propose a new non-iterative frequency-difference anomaly detection method called the factorization method (FM) and elaborate its physical justification. To demonstrate its practical applicability, we performed fdEIT phantom imaging experiments using a multi-frequency EIT system. Applying the FM to measured frequency-difference boundary voltage data sets, we could quantitatively evaluate indicator functions inside the imaging domain, of which values at each position reveal presence or absence of an anomaly. We found that the FM successfully localizes anomalies inside an imaging domain with a frequency-dependent complex conductivity distribution. We propose the new FM as an anomaly detection algorithm in fdEIT for potential applications in tumor and stroke imaging.**

***Index Terms*—Electrical impedance tomography (EIT), anomaly detection, factorization method, complex conductivity, weighted frequency difference**

I. Introduction

Electrical impedance tomography (EIT) aims to image a conductivity distribution inside the human body. As the complex conductivity values of biological tissues and organs are affected by their physiological and pathological status [1]–[3], EIT may open up new possibilities in medical diagnosis and monitoring of vital body functions. We may consider three imaging methods in EIT including static, time-difference, and frequency-difference imaging.

Static EIT aims to image absolute complex conductivity values inside the human body [4]–[7]. Its image reconstruction problem suffers from the fundamental ill-posedness combined with technical difficulties caused by modeling errors in boundary geometry and electrode positions.

Time-difference EIT (tdEIT) visualizes temporal changes in a complex conductivity distribution by using a difference in measured data at two different times. The subtraction diminishes errors and artifacts common to both data and tdEIT has been successfully applied to clinical settings where a time-reference data set is available [7]–[12]. For imaging or detection of tumor or acute stroke [13]–[16], tdEIT is not feasible since a time-reference data is not available.

Frequency-difference EIT (fdEIT) was proposed to image frequency-dependent changes of a complex conductivity distribution [17]–[26]. Most previous studies in fdEIT adopted a simple subtraction of voltage data at two different frequencies following the idea of tdEIT. When we assume an anomaly in a background whose complex conductivity distribution changes with frequency, this simple subtraction fails to cancel out common errors and artifacts at both frequencies. Based on this observation, a new fdEIT method using a weighted voltage difference has been suggested to diminish effects of common errors and artifacts [27].

Though weighted fdEIT has been validated by numerical simulations and phantom experiments [28], it still lacks a solid mathematical basis since there is no rigorous analysis on the connection between a complex conductivity perturbation and the weighted frequency-difference voltage data. To characterize the performance of a fdEIT image reconstruction algorithm, it is necessary to analyze this nonlinear connection. In this paper, we derive a constructive and quantitative physical correlation between weighted frequency-difference data and an anomaly. From this, we obtain a new and self-contained physical justification of the so-called factorization method (FM) [29]–[36], which is a non-iterative anomaly detection method. We propose a numerical algorithm that provides a criterion for determining presence or absence of an anomaly at each location in the imaging domain. The physical justification of the FM in fdEIT enables us to assess the performance of the anomaly detection algorithm in a practical environment. We present experimental results of applying the new FM to measured data sets from a conductivity phantom using a multi-frequency EIT system, KHU Mark1 [12], [37], [38].

B. Harrach (birth name: Bastian Gebauer) is with the Fakultät für Mathematik, Technische Universität München, Germany email: harrach@ma.tum.de

J. K. Seo is with the Department of Computational Science and Engineering, Yonsei University, Korea email: seoj@yonsei.ac.kr.

E. J. Woo is with the Department of Biomedical Engineering, Kyung Hee University, Korea email: ejwoo@khu.ac.kr.

This work was conducted while B. Harrach was employed at the Institut für Mathematik, Johannes Gutenberg-Universität Mainz, Germany and supported by the German Federal Ministry of Education and Research (BMBF) under grant 03HBPAM2 (Regularization techniques for electrical impedance tomography in medical and geological sciences). J. K. Seo was supported by the WCU program through NRF (R31-2008-000-10049-0). J. K. Seo and E. J. Woo were supported by the SRC/ERC program of MOST/NRF (R11-2002-103).

The distinguishability concept has played an important role to quantify the ability of a measured voltage data set in perceiving a difference between two conductivity images [39]. In this paper, we present an analysis about the detectability, which could be a basis for deeper understanding of the nonlinearity in EIT. We will show that it enables us to achieve better quantitative results in the fdEIT anomaly detection problem.

In section II, we describe a mathematical model for the weighted fdEIT. Section III contains the main contribution of the paper where we derive a constructive and quantitative physical correlation between a weighted frequency-difference voltage data set and a conductivity anomaly. This leads to a new physical justification of the FM and also an anomaly detection algorithm in a practical setting of fdEIT. In section IV, we describe how to numerically implement a variant of the FM for measured fdEIT data sets. Section V explains fdEIT experiments using a phantom comprising a background and anomalies whose complex conductivities vary with frequency. We illustrate experimental results by plotting indicator functions localizing anomalies. Validating the new detection algorithm with experimental fdEIT data sets, we propose further fdEIT studies to apply the method in tumor and acute stroke imaging.

II. Weighted Frequency-difference EIT

A. Problem Definition

Let $\Omega \subset \mathbb{R}^n$ ($n = 2$ or 3) denote a smooth domain occupying an electrically conducting object. We denote the complex conductivity at a position $x \in \Omega$ and angular frequency ω as $\gamma^\omega(x) = \sigma^\omega(x) + \mathrm{i}\omega\epsilon^\omega(\mathrm{x})$ where $\sigma^\omega(x)$ and $\epsilon^\omega(x)$ are conductivity and permittivity, respectively.

Using an N-channel multi-frequency EIT system, we attach N electrodes to the boundary $\partial\Omega$. We assume that the size of the electrodes is small compared to $\partial\Omega$, so that they can be modeled as *point electrodes* at positions $\xi_j \in \partial\Omega$, $j = 1, \ldots, N$. We inject sinusoidal current with a frequency of $\omega/2\pi$ and an amplitude of I between two adjacent electrodes ξ_j and ξ_{j+1}. In this paper, we use the convention $\xi_{N+1} = \xi_1$ and $\xi_0 = \xi_N$. The resulting complex potential u_j^ω is governed by the following partial differential equation:

$$\nabla \cdot (\gamma^\omega(x)\nabla u_j^\omega(x)) = 0 \quad \text{in } \Omega, \tag{1}$$

$$\gamma^\omega(x)\partial_\nu u_j^\omega(x)|_{\partial\Omega} = I\delta(x - \xi_j) - I\delta(x - \xi_{j+1}) \tag{2}$$

where $\delta(x)$ is the Dirac delta function and $\nu = \nu(x)$ is the outward unit normal vector on $\partial\Omega$.

We assume that the object Ω includes one or more anomalies occupying a region D in a homogeneous background so that

$$\gamma^\omega(x) = \gamma_0^\omega + \gamma_D^\omega(x)\chi_D(x) \tag{3}$$

where γ_0^ω is a background complex conductivity, $\gamma_D^\omega(x)$ a complex conductivity jump of the anomaly D, and χ_D its characteristic function. We sequentially inject currents between all pairs of adjacent electrodes and measure the resulting boundary voltages between adjacent electrode pairs excluding the two current-carrying electrodes for each injection. We are provided with the boundary voltage data $U_{j,k}^\omega = u_j^\omega(\xi_k) - u_j^\omega(\xi_{k+1})$ for $j, k = 1, \ldots, N$ and $k \notin \{j-1, j, j+1\}$ as shown in Fig. 1.

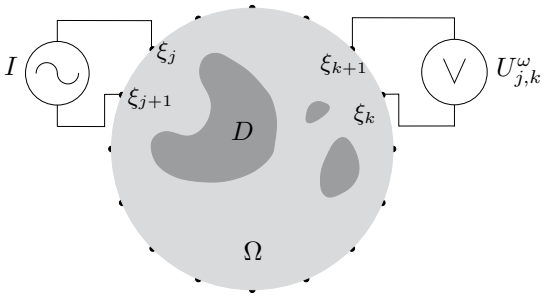

Fig. 1. Sketch of the measurement setup.

The measured boundary voltage data set is expressed in a data matrix as

$$\mathbf{U}^\omega = \begin{pmatrix} U_{1,1}^\omega & U_{1,2}^\omega & U_{1,3}^\omega & \ldots & U_{1,N}^\omega \\ U_{2,1}^\omega & U_{2,2}^\omega & U_{2,3}^\omega & \ldots & U_{2,N}^\omega \\ \vdots & \vdots & & \ddots & \vdots \\ U_{N,1}^\omega & U_{N,2}^\omega & U_{N,3}^\omega & \ldots & U_{N,N}^\omega \end{pmatrix} \tag{4}$$

where we fill the three missing entries of $U_{j,j-1}$, $U_{j,j}$ and $U_{j,j+1}$ by zero in each row, $j = 1, \ldots, N$. We can view the matrix $\mathbf{U}^\omega$ as a current-to-voltage or Neumann-to-Dirichlet (NtD) map. The problem of this paper is to identify the anomaly D from two data sets $\mathbf{U}^{\omega_1}$ and $\mathbf{U}^{\omega_2}$ measured at two different angular frequencies ω_1 and ω_2.

B. Weighted Frequency-difference Data

Scaling the complex conductivity $\gamma^\omega(x) \mapsto c\gamma^\omega(x)$ by a complex constant $c \in \mathbb{C}$ results in a data matrix scaled by c^{-1}, i.e., $\mathbf{U}^\omega \mapsto c^{-1}\mathbf{U}^\omega$. This means that $\gamma_0^\omega\mathbf{U}^\omega$ is the data that one would measure from a complex conductivity distribution of $1 + (\gamma_0^\omega)^{-1}\gamma_D^\omega(x)\chi_D(x)$.

We set a weighted frequency-difference data matrix $\mathbf{V}$ as

$$\mathbf{V} := \gamma_0^{\omega_1}\mathbf{U}^{\omega_1} - \gamma_0^{\omega_2}\mathbf{U}^{\omega_2}. \tag{5}$$

The first and second terms in the right hand side of (5) correspond to the following complex conductivity distributions

$$1+(\gamma_0^{\omega_1})^{-1}\gamma_D^{\omega_1}(x)\chi_D(x) \text{ and } 1+(\gamma_0^{\omega_2})^{-1}\gamma_D^{\omega_2}(x)\chi_D(x), \tag{6}$$

respectively. We note that the two complex conductivity distributions in (6) differ only on the anomaly D, that is, their complex conductivity distributions in the background $\Omega \setminus D$ are identical. This indicates that the weighted difference in (5) conveys anomaly information without being affected by the background. Numerical simulations and phantom experiments in [27], [28] provide comparative results between the simple and weighted differences.

We now derive a first analytic relation between $\mathbf{V}$ and the anomaly D. The (j, k)th entry of $\mathbf{V}$ is

$$V_{j,k} = v_j(\xi_k) - v_j(\xi_{k+1}) \quad \text{for} \quad j, k = 1, \ldots, N, \tag{7}$$

where $v_j(x) := \gamma_0^{\omega_1}u_j^{\omega_1}(x) - \gamma_0^{\omega_2}u_j^{\omega_2}(x)$ is the weighted frequency difference of the solutions $u_j^{\omega_1}(x)$ and $u_j^{\omega_2}(x)$ of (1), (2) with $\omega = \omega_1$ and ω_2, respectively.

From (1) and (3), we obtain

$$\begin{aligned}&\nabla\cdot(\gamma^{\omega_1}(x)\nabla v_j(x))\\&=\nabla\cdot\left(\gamma^{\omega_1}(x)\nabla\left(\gamma_0^{\omega_1}u_j^{\omega_1}(x)-\gamma_0^{\omega_2}u_j^{\omega_2}(x)\right)\right)\\&=\nabla\cdot\left(\gamma^{\omega_1}(x)\nabla\left(-\gamma_0^{\omega_2}u_j^{\omega_2}(x)\right)\right)\\&=\nabla\cdot\left(\left(\gamma^{\omega_2}(x)\gamma_0^{\omega_1}-\gamma^{\omega_1}(x)\gamma_0^{\omega_2}\right)\nabla u_j^{\omega_2}(x)\right)\\&=\nabla\cdot\left(\left(\gamma_0^{\omega_1}\gamma_D^{\omega_2}(x)-\gamma_0^{\omega_2}\gamma_D^{\omega_1}(x)\right)\chi_D(x)\nabla u_j^{\omega_2}(x)\right),\end{aligned}\tag{8}$$

in Ω. Equation (2) yields the insulated boundary condition

$$\partial_\nu v_j|_{\partial\Omega}=0\quad\text{ on }\partial\Omega.\tag{9}$$

The conductivity jump in the anomaly D has become a source term for the weighted frequency-difference potential v_j in (8).

From (2), Green's identity, and (1), we obtain

$$\begin{aligned}V_{j,k}&=v_j(\xi_k)-v_j(\xi_{k+1})\\&=\frac{1}{I}\int_{\partial\Omega}v_j(s)\gamma_0^{\omega_1}\partial_\nu u_k^{\omega_1}(s)\,\mathrm{d}s\\&=\frac{1}{I}\int_\Omega\gamma^{\omega_1}(x)\nabla v_j(x)\cdot\nabla u_k^{\omega_1}(x)\,\mathrm{d}x.\end{aligned}\tag{10}$$

We apply Green's identity again and use (8) and (9) to deduce

$$V_{j,k}=\frac{1}{I}\int_D(\gamma_0^{\omega_1}\gamma_D^{\omega_2}(x)-\gamma_0^{\omega_2}\gamma_D^{\omega_1}(x))\nabla u_j^{\omega_1}(x)\cdot\nabla u_k^{\omega_2}(x)\,\mathrm{d}x.\tag{11}$$

This means that we may interpret $V_{j,k}$ as a response of the anomaly D to the potential $u_j^{\omega_1}$ resulting from a current at ω_1 between the jth and $(j+1)$th electrodes and the potential $u_k^{\omega_2}$ resulting from a current at ω_2 between the kth and $(k+1)$th electrodes.

By superposition, it follows that for any two vectors $g,h\in\mathbb{C}^N$,

$$\begin{aligned}g\cdot\mathbf{V}h&=\sum_{j,k=1}^N g_jV_{j,k}h_k\\&=\frac{1}{I}\int_D\left(\gamma_0^{\omega_1}\gamma_D^{\omega_2}(x)-\gamma_0^{\omega_2}\gamma_D^{\omega_1}(x)\right)\nabla u_g^{\omega_1}(x)\cdot\nabla u_h^{\omega_2}(x)\,\mathrm{d}x\end{aligned}\tag{12}$$

where $u_g^{\omega_1}=\sum_{j=1}^N g_ju_j^{\omega_1}$ is a potential resulting from the sum of currents of the strength g_j between the jth and $(j+1)$th electrodes and $u_h^{\omega_2}$ is defined similarly. In section III, we will apply this analytic relation to determine points inside the anomaly D.

Assuming that $\gamma_D^{\omega_1}(x)$ and $\gamma_D^{\omega_2}(x)$ are small, we get

$$\nabla u_k^{\omega_j}(x)\approx\frac{1}{\gamma_0^{\omega_j}}\nabla u_k^{(0)}(x)\tag{13}$$

where $u_k^{(0)}$ is the potential in Ω with $\gamma=1$ subject to an injection current of I between the kth and $(k+1)$th electrodes. Since the same holds for $u_j^{\omega_2}$,

$$V_{j,k}\approx\frac{1}{I}\int_D\left(\frac{\gamma_D^{\omega_2}(x)}{\gamma_0^{\omega_2}}-\frac{\gamma_D^{\omega_1}(x)}{\gamma_0^{\omega_1}}\right)\nabla u_j^{(0)}(x)\cdot\nabla u_k^{(0)}(x)\,\mathrm{d}x\tag{14}$$

and an analogous expression holds for $g\cdot\mathbf{V}h$.

C. Contrast in Frequency-difference EIT

The contrast in fdEIT essentially depends on $\gamma_D^{\omega_2}(x)/\gamma_0^{\omega_2}-\gamma_D^{\omega_1}(x)/\gamma_0^{\omega_1}$ in (14). Note that the same term appears in (8), (11), and (12) up to multiplicative constants. For general biological tissues showing complicated frequency dependent characteristics, we cannot simplify this term.

To obtain a useful interpretation, we consider a simplifying assumption that both σ and ϵ do not change with frequency and both $\gamma_D^{\omega_1}$ and $\gamma_D^{\omega_2}$ are constant. Then,

$$\gamma^{\omega_j}(x)=\sigma(x)+\mathrm{i}\omega_j\epsilon(x)\quad\text{for}\quad j=1,2,\tag{15}$$

$$\sigma(x)=\sigma_0+\sigma_D\chi_D(x),\tag{16}$$

$$\epsilon(x)=\epsilon_0+\epsilon_D\chi_D(x),\tag{17}$$

and

$$\frac{\gamma_D^{\omega_2}(x)}{\gamma_0^{\omega_2}}-\frac{\gamma_D^{\omega_1}(x)}{\gamma_0^{\omega_1}}=\frac{\mathrm{i}}{\gamma_0^{\omega_1}\gamma_0^{\omega_2}}(\omega_2-\omega_1)(\epsilon_D\sigma_0-\sigma_D\epsilon_0).\tag{18}$$

The contrast increases with the frequency gap $\omega_2-\omega_1$ and fdEIT is capable of imaging a purely dielectric anomaly ($\sigma_D=0\neq\epsilon_D$) as well as a purely conducting anomaly ($\sigma_D\neq0=\epsilon_D$). Irrespective of frequency, the factor $\epsilon_D\sigma_0-\sigma_D\epsilon_0$ may be zero when jumps in σ and ϵ are exactly same. In such a rare case, the weighted frequency-difference data in (5) is zero, and the anomaly is invisible from the data.

III. Anomaly Detection

We now derive a constructive and quantitative physical correlation between the weighted frequency-difference data $\mathbf{V}$ and the anomaly D. Our arguments stem from a non-iterative anomaly detection method called the factorization method (FM) and its variant called the linear sampling method (LSM). Mathematically rigorous treatments of these methods are available in [29]–[36]. In the mathematical literature, they are analyzed for the idealized case of continuous boundary measurements. Their rigorous mathematical descriptions are beyond the scope of this paper (see e.g. [36] for the case of fdEIT).

In this section, we provide a self-contained analysis and description of the FM and LSM bearing their practical applications in mind. We will explain a new physical justification of these methods for the anomaly detection using fdEIT. We start by introducing a main tool to correlate an anomaly with boundary data. We will derive the correlation for the linearized case first and then for the nonlinear case.

A. Electric Dipole Source

Consider an electric potential $\varphi_{z,d}$ in a homogeneous domain Ω subject to a dipole source at a point $z\in\Omega$ with a direction d. It satisfies

$$\nabla^2\varphi_{z,d}(x)=d\cdot\nabla\delta(x-z),\quad x\in\Omega\tag{19}$$

with the insulated boundary condition $\partial_\nu\varphi_{z,d}(x)|_{\partial\Omega}=0$ on $\partial\Omega$. For the setup in section II, such a dipole source would give rise to the following voltage measurements

$$\Phi_{z,d}=\begin{pmatrix}\varphi_{z,d}(\xi_1)-\varphi_{z,d}(\xi_2)\\\vdots\\\varphi_{z,d}(\xi_N)-\varphi_{z,d}(\xi_1)\end{pmatrix}\in\mathbb{R}^N.\tag{20}$$

By the same arguments as in the derivation of (11), the kth component of $\Phi_{z,d}$ is the same as $d \cdot \nabla u_k^{(0)}(z)$ where $u_k^{(0)}(x)$ is the potential in Ω with $\gamma = 1$ subject to an injection current between the kth and $(k+1)$th electrodes.

B. Anomaly Detection: Linearized Case

We derive a physical correlation between the data $\mathbf{V}$ and the anomaly D under the assumption that $\gamma_D^{\omega_1}(x)$ and $\gamma_D^{\omega_2}(x)$ are small so that the linearized equation (14) holds. Without loss of generality, we assume that $I = 1$. We denote by $\mathbf{V}^{-1}$ the pseudo-inverse of $\mathbf{V}$ and assume that $h_{z,d} = \mathbf{V}^{-1}\Phi_{z,d}$ is a current pattern for which the voltage measurements agree with those of the dipole, i.e., $\mathbf{V}h_{z,d} = \Phi_{z,d}$. Note that such a current pattern will only exist if $\Phi_{z,d}$ lies in the range of $\mathbf{V}$. We will later replace $\mathbf{V}$ by its real part and then this property can be guaranteed, cf. our remark at the end of this section.

By using superposition and (14), we obtain

$$\begin{aligned} d \cdot \nabla u_g^{(0)}(z) &= g \cdot \Phi_{z,d} = g \cdot \mathbf{V} h_{z,d} \qquad (21)\\ &\approx \int_D \left(\frac{\gamma_D^{\omega_2}(x)}{\gamma_0^{\omega_2}} - \frac{\gamma_D^{\omega_1}(x)}{\gamma_0^{\omega_1}} \right) \nabla u_g^{(0)}(x) \cdot \nabla u_{h_{z,d}}^{(0)}(x)\ \mathrm{d}x \end{aligned}$$

for all vectors $g \in \mathbb{C}^N$. It follows from the Schwartz inequality that

$$\begin{aligned} &\left| d \cdot \nabla u_g^{(0)}(z) \right| \qquad (22)\\ &\leq \sqrt{\int_D \left| \frac{\gamma_D^{\omega_2}}{\gamma_0^{\omega_2}} - \frac{\gamma_D^{\omega_1}}{\gamma_0^{\omega_1}} \right|^2 |\nabla u_{h_{z,d}}^{(0)}|^2 \mathrm{d}x} \sqrt{\int_D |\nabla u_g^{(0)}|^2 \mathrm{d}x}. \end{aligned}$$

Since (22) holds for all $g \in \mathbb{C}^N$, we have

$$\begin{aligned} &\max_{g \in \mathbb{C}^N} \frac{|d \cdot \nabla u_g^{(0)}(z)|}{\sqrt{\int_D |\nabla u_g^{(0)}(x)|^2 \mathrm{d}x}} \qquad (23)\\ &\leq \sqrt{\int_D \left| \frac{\gamma_D^{\omega_2}}{\gamma_0^{\omega_2}} - \frac{\gamma_D^{\omega_1}}{\gamma_0^{\omega_1}} \right|^2 \left| \nabla u_{h_{z,d}}^{(0)} \right|^2 \mathrm{d}x}. \end{aligned}$$

We call a point $z \notin D$ *well-separated* from D if there is a current pattern g for which the ratio

$$\frac{|d \cdot \nabla u_g^{(0)}(z)|}{\sqrt{\int_D |\nabla u_g^{(0)}(x)|^2 \mathrm{d}x}} \qquad (24)$$

is very large for some direction d, i.e., if the current flux resulting from g is very small in D but very large at z in some direction (see figure 2). Note that this depends not only on the distance between z and D but also on their relative locations. Since the right hand side of (23) depends continuously on $h_{z,d}$, $\|h_{z,d}\| = \|\mathbf{V}^{-1}\Phi_{z,d}\|$ is large for all z that are *well-separated* from D. A plot of $\|\mathbf{V}^{-1}\Phi_{z,d}\|$ is likely to reveal the anomaly and this is the discrete version of the LSM.

These arguments explain why $\|h_{z,d}\|$ is large when z is well-separated from D, but they do not explain why it should be small inside D. To gain a better indicator for presence or absence of the anomaly, one has to use additional definiteness properties. We replace $\mathbf{V}$ by a matrix $\Re(\mathbf{V})$ containing only real parts of the entries of $\mathbf{V}$ and let $h_{z,d} = \Re(\mathbf{V})^{-1}\Phi_{z,d}$.

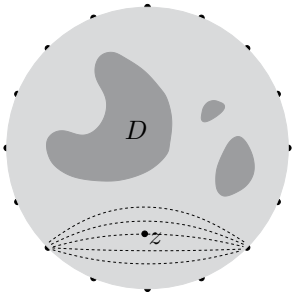

Fig. 2. Large current flows through a point z that is well separated from the almost current-free anomaly D.

Suppose that there are two positive constants c_* and c^* such that

$$c_* \leq \Re\left(\frac{\gamma_D^{\omega_2}(x)}{\gamma_0^{\omega_2}} - \frac{\gamma_D^{\omega_1}(x)}{\gamma_0^{\omega_1}} \right) \leq c^*, \quad x \in D. \qquad (25)$$

From (23), we have

$$\frac{1}{c^*} \max_{g \in \mathbb{R}^N} \frac{|d \cdot \nabla u_g^{(0)}(z)|}{\|\nabla u_g^{(0)}\|_D} \ \leq\ \|\nabla u_{h_{z,d}}^{(0)}\|_D. \qquad (26)$$

Hence, $\|\nabla u_{h_{z,d}}^{(0)}\|_D$ must be large for a point z that is well-separated from D.

We now consider the case when $z \in D$. From (14) and superposition, we obtain

$$\begin{aligned} d \cdot \nabla u_{h_{z,d}}^{(0)}(z) &= h_{z,d} \cdot \Re(\mathbf{V}) h_{z,d} \qquad (27)\\ &\approx \int_D \Re\left(\frac{\gamma_D^{\omega_2}(x)}{\gamma_0^{\omega_2}} - \frac{\gamma_D^{\omega_1}(x)}{\gamma_0^{\omega_1}} \right) |\nabla u_{h_{z,d}}^{(0)}(x)|^2\ \mathrm{d}x. \end{aligned}$$

The consequences of (27) are twofold. The first is

$$c_* \|\nabla u_{h_{z,d}}^{(0)}\|_D^2 \leq d \cdot \nabla u_{h_{z,d}}^{(0)}(z). \qquad (28)$$

If $z \in D$ and the distance between z and ∂D is r, it follows from the mean value property of the harmonic function $d \cdot \nabla u_{h_{z,d}}^{(0)}(z)$ that

$$d \cdot \nabla u_{h_{z,d}}^{(0)}(z) \leq \frac{1}{c_r} \|\nabla u_{h_{z,d}}^{(0)}\|_D \qquad (29)$$

where c_r is the square root of the volume of the ball with radius r, and so

$$\|\nabla u_{h_{z,d}}^{(0)}(x)\|_D \leq \frac{1}{c_* c_r}. \qquad (30)$$

The second consequence is that

$$\|\Re(\mathbf{V})^{-1/2}\Phi_{z,d}\| = \Phi_{z,d} \cdot \Re(\mathbf{V})^{-1}\Phi_{z,d} = h_{z,d} \cdot \Re(\mathbf{V}) h_{z,d} \qquad (31)$$

fulfills

$$c_* \|\nabla u_{h_{z,d}}^{(0)}(x)\|_D^2 \leq h_{z,d} \cdot \Re(\mathbf{V}) h_{z,d} \leq c^* \|\nabla u_{h_{z,d}}^{(0)}(x)\|_D^2. \qquad (32)$$

Here, $\Re(\mathbf{V})^{1/2}$ denotes the matrix-valued square root of the positive-semidefinite symmetric real matrix $\Re(\mathbf{V})$.

By combining the estimates (26), (30), and (32), we have the following (for all directions d):

- If $z \in D$ and the distance between z and ∂D is r, then

$$\left| \Phi_{z,d} \cdot \Re(\mathbf{V})^{-1}\Phi_{z,d} \right| \leq \frac{c^*}{(c_* c_r)^2}. \qquad (33)$$

- If $z \notin D$, then

$$\left|\Phi_{z,d} \cdot \Re(\mathbf{V})^{-1} \Phi_{z,d}\right| \geq \frac{c_*}{(c^*)^2} \left(\max_{g \in \mathbb{R}^N} \frac{|d \cdot \nabla u_g^{(0)}(z)|}{\|\nabla u_g^{(0)}\|_D} \right)^2. \tag{34}$$

For the case where the contrast (25) is negative and bounded from above by a negative constant, the same arguments hold true with $-\Re(\mathbf{V})^{-1}$ instead of $\Re(\mathbf{V})^{-1}$. We can combine both cases by replacing $\Re(\mathbf{V})$ with its matrix-valued absolute value $|\Re(\mathbf{V})|$.

The quantity

$$\left|\Phi_{z,d} \cdot |\Re(\mathbf{V})|^{-1} \Phi_{z,d}\right| \tag{35}$$

is small inside the anomaly D and large at all points $z \notin D$ that are well-separated from D. Plotting this quantity will therefore reveal the inclusion and this is the discrete version of the FM. Note that in the estimates (30) and (32), all the quantities except c_* and c^* are computable. If we have *a priori* knowledge about c_* and c^* (anomaly conductivity contrast), we can determine presence or absence of the anomaly at each location z with a quantitative confidence level unless the size of the anomaly is too small.

C. Anomaly Detection: Nonlinear Case

We can follow the arguments in section III-B without linearization. Using (12) instead of its linearized version, we obtain

$$\begin{aligned} d \cdot \nabla u_g^{(0)}(z) &= g \cdot \Phi_{z,d} = g \cdot \mathbf{V} h_{z,d} \\ &= \int_D \left(\frac{\gamma_D^{\omega_2}(x)}{\gamma_0^{\omega_2}} - \frac{\gamma_D^{\omega_1}(x)}{\gamma_0^{\omega_1}} \right) \nabla u_g^{\omega_1}(x) \cdot \nabla u_{h_{z,d}}^{\omega_2}(x) \, \mathrm{d}x \end{aligned} \tag{36}$$

for all vectors $g \in \mathbb{C}^N$. Up to multiplicative constants, the quantity $\|\nabla u_g^{\omega_1}\|_D$ can be estimated from above and below by $\|\nabla u_g^{(0)}\|_D$. For $\gamma = \sigma$ (real), this follows from [40, Lemma 2.1] and [40, Lemma 2.5], and the same proof holds for $\gamma = \sigma + \mathrm{i}\omega\epsilon$ (complex). With the same arguments as in section III-B, $h_{z,d}$ must hence be large for all points that are well-separated from the anomaly D. The LSM indicator function holds for the nonlinear case too.

Furthermore, (27) must be replaced by

$$\begin{aligned} d \cdot \nabla u_{h_{z,d}}^{(0)}(z) &= \overline{h_{z,d}} \cdot \Re(\mathbf{V}) h_{z,d} \\ &= \int_D \Re \left(\frac{\gamma_D^{\omega_2}(x)}{\gamma_0^{\omega_2}} - \frac{\gamma_D^{\omega_1}(x)}{\gamma_0^{\omega_1}} \right) \nabla u_{h_{z,d}}^{\omega_1}(x) \cdot \nabla u_{h_{z,d}}^{\omega_2}(x) \, \mathrm{d}x. \end{aligned} \tag{37}$$

Under appropriate assumptions on the contrast, the right hand side of (37) is bounded from above and below up to multiplicative constants by $\|\nabla u_{h_{z,d}}^{(0)}(x)\|_D^2$ for the case of continuous boundary measurements [36]. Since the same arguments hold for the case of a finite number of electrodes, all the arguments in section III-B can be carried over to the nonlinear case, which justifies the FM indicator function in the nonlinear case also.

From the same bound it also follows that the nullspace of $\Re(\mathbf{V})$ consists of the vectors with constant entries. Since the entries of Φ_z sum up to zero, Φ_z lies orthogonal to this nullspace. Hence, by symmetry of $\Re(\mathbf{V})$, it follows that Φ_z lies in the range of $\Re(\mathbf{V})$.

IV. Numerical Implementation

We assume two measurement matrices $\mathbf{U}^{\omega_1}$ and $\mathbf{U}^{\omega_2}$ at two different frequencies as described in section II-A. To form the weighted frequency-difference data matrix $\mathbf{V}$, we first estimate the unknown background complex conductivity from the data. We proceed similar to [27] and note that $\mathbf{U}^{\omega_j}$ is approximately proportional to $(\gamma_0^{\omega_j})^{-1}$. An estimate of $\gamma_0^{\omega_j}$ up to a real constant is $c_j := 1 - \alpha_j \mathrm{i}$ where α_j solves the following quadratic minimization problem:

$$\min \|\alpha_j \Re(\mathbf{U}^{\omega_j}) - \Im(\mathbf{U}^{\omega_j})\|. \tag{38}$$

The minimizer is given by

$$\alpha_j = \Re(\mathbf{U}^{\omega_j}) : \Im(\mathbf{U}^{\omega_j}) / \left(\Re(\mathbf{U}^{\omega_j}) : \Re(\mathbf{U}^{\omega_j})\right) \tag{39}$$

where ":" denotes the double dot matrix inner product. Since we set the unreliable entries of $U_{k,k-1}^{\omega_j}$, $U_{k,k}^{\omega_j}$, and $U_{k,k+1}^{\omega_j}$ in each row by zero, they have no effect in the calculation of α_j.

Assuming that the conductivity σ does not change with frequency, both estimates c_1 and c_2 differ from $\gamma_0^{\omega_1}$ and $\gamma_0^{\omega_2}$ by the same real constant. We can take $\mathbf{M} := \Re(c_1 \mathbf{U}^{\omega_1} - c_2 \mathbf{U}^{\omega_2})$ as an estimate for $\Re(\mathbf{V})$ used in the FM. According to section II-C, the sign of the contrast depends only on the sign of $\omega_1 - \omega_2$. This allows us to utilize voltage data at more than two frequencies to increase the contrast. For this, we take $\mathbf{M}$ as the sum of real parts of several sorted pairs of weighted frequency-difference voltages.

In every row of $\mathbf{M}$, three values of $M_{j,j-1}$, $M_{j,j}$, and $M_{j,j+1}$ are zero. This has a rather drastic effect destroying the definiteness property of $\mathbf{M}$ that the FM relies on. Taking the matrix-valued absolute value $|\mathbf{M}|$ restores this definiteness. Though we have observed the method working well with this simple heuristic approach, more elaborate strategies to deal with these unreliable entries may further enhance the performance and should be the subject of further studies.

We now turn to the dipole function. For special geometries, solutions of (19) are known explicitly. For the two-dimensional unit circle, it is given by [33] as

$$\varphi_{z,d} = \frac{1}{\pi} \frac{(z-x) \cdot d}{|z-x|^2}, \tag{40}$$

so that $\Phi_{z,d}$ is obtained from (20). For more complicated geometries, $\Phi_{z,d}$ can be calculated by solving the homogeneous forward problems for every pair of adjacent currents and using the first equality in (21).

In the idealized case of complete boundary measurements using inifinitely many electrodes, an arbitrary dipole direction d can be taken. In our practical setting, d determines the direction in which the localized current flux is orientated. Depending on the position of the point relative to the electrodes, the current flux has a preferred direction. To obtain a symmetric indicator, we combine dipoles in all orthogonal basis directions $e_k \in \mathbb{R}^n$, by taking the sum of squared respective indicator functions. We normalize the indicator functions with respect to the dipole norm. Best results are usually obtained by plotting the indicator functions in the

logarithmic scale. We plot

$$\log\left(1+\frac{\overline{\Phi_{z,e_1}}\cdot|\mathbf{M}|^{-1}\Phi_{z,e_1}+\ldots+\overline{\Phi_{z,e_n}}\cdot|\mathbf{M}|^{-1}\Phi_{z,e_n}}{\overline{\Phi_{z,e_1}}\cdot\Phi_{z,e_1}+\ldots+\overline{\Phi_{z,e_n}}\cdot\Phi_{z,e_n}}\right) \tag{41}$$

as a function of $z\in\Omega$.

Note that we have implemented $|\mathbf{M}|^{-1}\Phi_{z,d}$ without any regularization and this works reasonably well for the practically important case of a small number of electrodes. When the number of electrodes gets larger, the matrix $\mathbf{M}$ becomes ill-conditioned and the calculation of $|\mathbf{M}|^{-1}\Phi_{z,d}$ requires a regularization method to prevent an excessive amplification of measurement noise.

V. Frequency-difference EIT Experiments

A. Experimental Setup

We tested our new anomaly detection algorithm based on the FM on the same data sets described in [28]. The imaging object was a cylindrical phantom of 200 mm diameter and 100 mm height. We placed 16 equally spaced electrodes around the phantom to create a physical model of the two-dimensional unit circle with 16 equally spaced point electrodes. As described in section II-A, current injections and voltage measurements were carried out at chosen frequencies of 1, 5, 10, 50, 100, 250, and 500 kHz using a 16-channel multi-frequency EIT system KHU Mark1 [12], [37], [38]. In order to simulate a realistic complex conductivity distribution of organic tissues, we filled the phantom by 0.5% saline background (B1), by a mixture of carrot pieces with 1% saline (B2), and by macerated banana (B3). As anomalies we used cylindrical pieces of banana (A1) and carrot (A2). Table I summarizes the measured complex conductivity values of the five materials used in the imaging experiments. Complex conductivity values at other frequencies are reported in Oh *et al.* [12].

B. Experimental Results

As described in section IV, we combined several pairs of frequencies by adding up respective real parts of the weighted frequency-difference voltages. Fig. 3 shows the results for the following six configurations:

(a) a banana anomaly (A1) placed in the background of the mixture of 1% saline and carrot pieces (B2),
(b) a carrot anomaly (A2) placed in the background of macerated banana (B3),
(c) two anomalies of carrot and banana (A1 and A2) placed in the background of the mixture of 1% saline and carrot pieces (B2),
(d) two anomalies of banana and carrot (A1 and A2) placed in the background of macerated banana (B3),
(e) two anomalies of carrot and banana (A1 and A2) placed in the 0.5% saline background (B1),
(f) four banana anomalies (A1) placed in the background of the mixture of 1% saline and carrot pieces (B2).

The middle column of Fig. 3 plots the indicator functions without thresholding. The anomalies in (a)–(c) are reconstructed relatively well. In (d) and (e), the carrot anomaly appears to be more prominent than the banana anomaly. In (e), the contrast discussed in section II-C depends only on the permittivity of the anomalies since the saline background has a negligible permittivity effect. In (f), all four banana anomalies are reconstructed but the indicator function is significantly high in the central area surrounded by them. This effect can be explained by our physical justification of the FM. For those points surrounded by the four banana anomalies, the current flux can hardly be made large without making it large also inside the banana anomalies.

VI. Discussion

Though the anomalies are visually spotted in the indicator plots shown in the middle columns of Fig. 3, it is not clear how to fix a threshold value for segmenting the anomaly region from the domain. According to estimates (33) and (34), it would be difficult to fix a threshold when the sizes of the anomalies are very small. In the right columns of Fig. 3, we show plots of the indicator functions with its scale bar cropped to the lower 15%, which visualize the anomalies rather well in some cases. We have chosen the cropping parameter with the true anomalies' locations in mind which may be regarded as *tweaking crime* (changing the cropping parameter setting to improve performance) according to [41]. Since the same cropping works well for different experiments, we do however expect that the necessary threshold can be chosen empirically in practice.

Comparing measured complex conductivity values in Table I and the indicator plots in Fig. 3, we can see that the FM supplies information about the detectability of an anomaly not about the actual contrast in complex conductivity values. We may take advantage of the shape information from the FM to improve the image quality using conventional reconstruction methods. The middle columns of Fig. 4 show standard linearized reconstructions that we obtained by discretizing the linearized equation (14), and solving the resulting linear system using the Tikhonov regularization. In the right columns, we used the indicator function (41) as a pixelwise weight for the Tikhonov regularization term. Consequently, the lower the chance of presence of an anomaly is in some region (according to the FM), the more regularization is being applied in that region. For both methods, only a single frequency pair, 5 and 50 kHZ, was used and the regularization parameters were chosen by hand for one of the examples and then kept the same for all others. This simple combination strategy improves the shape of the reconstructed inclusions and lessens boundary artifacts, especially in the case of multiple inclusions.

The focus of this work is on the justification of the factorization method as an anomaly detection algorithm and we did not conduct an accurate error analysis of this simple combination strategy. Nevertheless let us try to give a very rough quantification of the possible improvements in terms of background smoothness and anomaly shape accuracy. The black circles in Fig. 4 show rough estimates of the true inclusions that we obtained by manually estimating the inclusions radii to be approximately one sixth of that of the phantom and positioning their centers in the middle between local

This is the accepted version of an article that has been published in
IEEE Transactions on Medical Imaging 29 (11), 1918-1926, 2010 (http://dx.doi.org/10.1109/TMI.2010.2053553) ©IEEE

TABLE I
MEASURED COMPLEX CONDUCTIVITY VALUES AT 1, 5 AND 50 KHZ.

	Measured complex conductivity in S/m									
	saline background (B1)		carrot background (B2)		banana background (B3)		banana anomaly (A1)		carrot anomaly (A2)	
	σ	$\omega\epsilon$	σ	$\omega\epsilon$	σ	$\omega\epsilon$	σ	$\omega\epsilon$	σ	$\omega\epsilon$
1 kHz	0.130	0	0.208	0.102	0.221	0.109	0.023	0.011	0.035	0.016
5 kHz	0.130	0	0.208	0.103	0.228	0.110	0.031	0.012	0.043	0.017
50 kHz	0.130	0	0.232	0.123	0.283	0.150	0.100	0.050	0.102	0.052

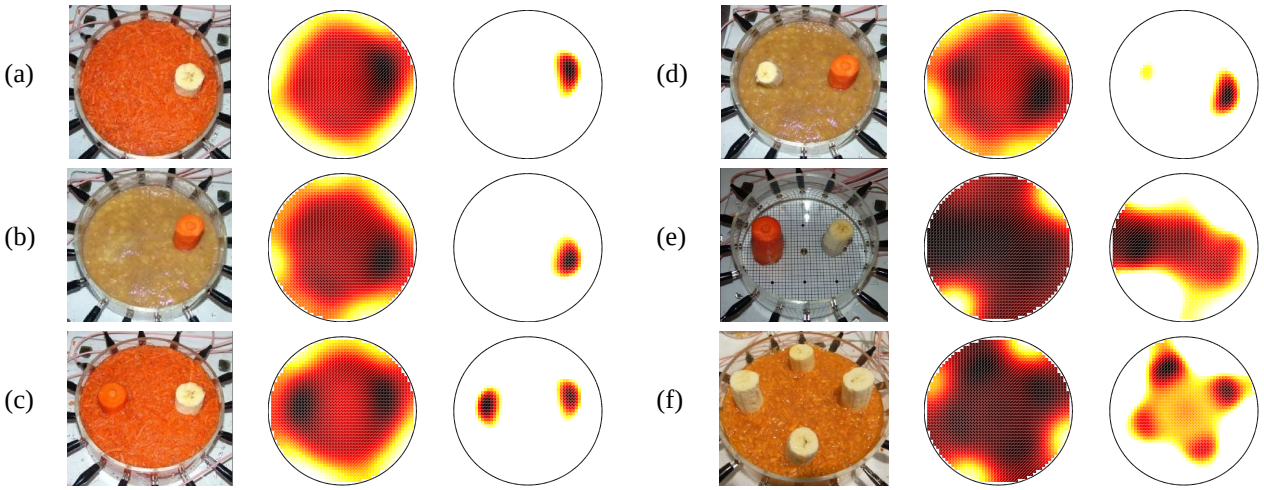

Fig. 3. Measurement setups (left column), reconstructions using all available weighted frequency differences with full color axis (middle column), and with color axis cropped to lower 15% (right column).

maxima in the reconstructions. Then we normalized the values to the unit interval and calculated the variance of the values outside the inclusions as a measure of background smoothness, see table II. In all examples, the background variance in the FM-weighted reconstructions is lowered by at least 20%. To estimate shape accuracy we compared the level set of the medium value 0.5 in the reconstructions with the inclusions shape and counted the relative number of wrongly associated pixels, see again table II. In all examples, the FM-weight almost halves this number.

Let us however note that certain effects are not visible in the rough quantitative estimates in table II. In example (f) the reconstructions using the FM-weight look slightly elongated into the center of the domain, which may be caused by the above explained difficulties of the FM to distinguish a point surrounded by anomalies from a point inside the anomalies. More elaborate ways of combining the FM with linearized strategies will surely lead to further enhancements and will be the subject of further studies. For an idealized theoretical setting, Harrach and Seo proved that it is possible to enhance linearized strategies by globally convergent shape reconstruction properties [42]. For more numerical results on combining the FM and linearized reconstructions including a detailed description of the implementation, we refer the reader to [43].

TABLE II
ROUGH ESTIMATE OF THE IMPROVEMENTS IN BACKGROUND SMOOTHNESS AND SHAPE ACCURACY OBTAINED BY FM-WEIGHTED REGULARIZATION.

	Background variance		Shape error	
	Standard	FM-weighted	Standard	FM-weighted
(a)	0.0101	0.0078	13.9%	5.3%
(b)	0.0130	0.0094	8.6%	3.7%
(c)	0.0143	0.0113	27.6%	11.4%
(d)	0.0180	0.0127	15.2%	7.4%
(e)	0.0107	0.0048	4.1%	2.1%
(f)	0.0136	0.0106	16.5%	4.3%

VII. CONCLUSION

We have derived a constructive and quantitative physical correlation between a frequency-difference boundary voltage data set and a conductivity anomaly. This enabled us to physically justify the FM in fdEIT and develop a new anomaly detection method. Numerically implementing the method and performing fdEIT phantom experiments, we could assess its performance in a practical setting of fdEIT.

Without any *a priori* information or empirical knowledge on sizes of anomalies, the method can indicate only their locations. In this sense, the scope of the FM stays qualitative not quantitative. The more electrodes are used, the better the current flux can be concentrated or localized at points outside the anomaly D. This will help the indicator functions to visualize the anomaly more clearly assuming that we can accurately measure a small voltage difference between a pair of closely positioned electrodes. When a point is surrounded by anomalies, one cannot concentrate the current flux at the point without also raising the current flux through the anomalies. In such a case, the point may wrongly be identified as an anomaly.

Though the interpretation of the data set as a matrix or

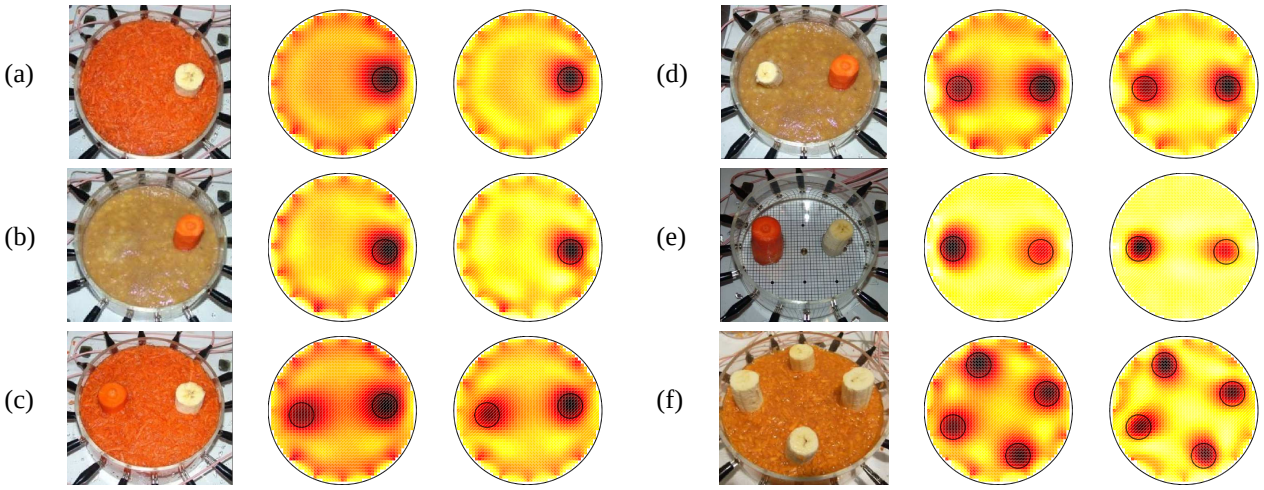

Fig. 4. Measurement setups (left column), linearized reconstructions with standard Tikhonov regularization (middle column), and with FM-weighted Tikhonov regularization(right column).

operator arguably makes the method not easily accessible from a practical point of view, our numerical implementation and experimental results verified that the new method is practically feasible. The analysis presented in this paper could be a basis for deeper understanding of the effect of nonlinearity in EIT, which is often ignored in difference imaging methods. In future studies, we hope to achieve more quantitative results for evaluating the detectability of an anomaly in fdEIT. We plan to undertake comparative studies with other anomaly detection methods for the experimental validation of the FM in fdEIT.

REFERENCES

[1] L. A. Geddes and L. E. Baker, "The specific resistance of biological material: a compendium of data for the biomedical engineer and physiologist," *Med. Biol. Engng.*, vol. 5, pp. 271–293, 1967.

[2] S. Gabriel, R. W. Lau, and C. Gabriel, "The dielectric properties of biological tissues: Ii. measurements in the frequency range 10 hz to 20 ghz," *Phys. Med. Biol.*, vol. 41, pp. 2251–2269, 1996.

[3] S. Grimnes and O. G. Martinsen, *Bioimpedance and Bioelectricity Basics, 2nd. ed.* Oxford, UK: Academic Press, 2008.

[4] T. J. Yorkey, J. G. Webster, and W. J. Tompkins, "Comparing reconstruction algorithms for electrical impedance tomography," *IEEE Trans. Biomed. Eng.*, vol. BME-34, pp. 843–852, 1987.

[5] E. J. Woo, P. Hua, J. G. Webster, and W. J. Tompkins, "A robust image reconstruction algorithm and its parallel implementation in electrical impedance tomography." *IEEE Trans. Med. Imag.*, vol. 12, pp. 137–146, 1993.

[6] D. Isaacson, J. L. Mueller, J. C. Newell, and S. Siltanen, "Reconstructions of chest phantoms by the d-bar method for electrical impedance tomography," *IEEE Trans. Biomed. Eng.*, vol. 23, pp. 821–828, 2004.

[7] D. Holder, *Electrical Impedance Tomography: Methods, History and Applications*. Bristol, UK: IOP Publishing, 2005.

[8] D. C. Barber and B. H. Brown, "Applied potential tomography," *J. Phys. E: Sci. Instrum.*, vol. 17, pp. 723–733, 1984.

[9] M. Cheney, D. Isaacson, J. C. Newell, S. Simske, and J. Goble, "NOSER: an algorithm for solving the inverse conductivity problem," *Int. J. Imag. Syst. Tech.*, vol. 2, pp. 66–75, 1990.

[10] P. Metherall, D. C. Barber, R. H. Smallwood, and B. H. Brown, "Three-dimensional electrical impedance tomography," *Nature*, vol. 380, pp. 509–512, 1996.

[11] M. Cheney, D. Isaacson, and J. C. Newell, "Electrical impedance tomography," *SIAM Rev.*, vol. 41, no. 1, pp. 85–101, 1999.

[12] T. I. Oh, W. Koo, K. H. Lee, S. M. Kim, J. Lee, S. W. Kim, J. K. Seo, and E. J. Woo, "Validation of a multi-frequency electrical impedance tomography (mfEIT) system KHU Mark1: impedance spectroscopy and time difference imaging," *Physiol. Meas.*, vol. 29, pp. 295–307, 2008.

[13] N. K. Soni, A. Hartov, C. Kogel, S. P. Poplack, and K. D. Paulsen, "Multi-frequency electrical impedance tomography of the breast: new clinical results," *Physiol. Meas.*, vol. 25, pp. 301–314, 2004.

[14] A. McEwan, A. Romsauerova, R. Yerworth, L. Horesh, R. Bayford, and D. Holder, "Design and calibration of a compact multi-frequency eit system for acute stroke imaging," *Physiol. Meas.*, vol. 27, pp. S199–210, 2006.

[15] R. Kulkarni, G. Boverman, D. Isaacson, G. J. Saulnier, T. Kao, and J. C. Newell, "An analytical layered forward model for breasts in electrical impedance tomography," *Physiol. Meas.*, vol. 29, pp. S27–40, 2008.

[16] O. V. Trokhanova, M. B. Okhapkin, and A. V. Korjenevsky, "Dual-frequency electrical impedance mammography for the diagnosis of non-malignant breast disease," *Physiol. Meas.*, vol. 29, pp. S331–344, 2008.

[17] H. Griffiths and A. Ahmed, "A dual-frequency applied potential tomography technique: computer simulations," *Clin. Phys. Physiol. Meas.*, vol. 8, pp. 103–107, 1987.

[18] H. Griffiths, H. T. L. Leung, and R. J. Williams, "Imaging the complex impedance of the thorax," *Clin. Phys. Physiol. Meas.*, vol. 13 (Supplement A), pp. 77–82, 1992.

[19] J. Jossinet and C. Trillaud, "Imaging the complex impedance in eit," *Clin. Phys. Physiol. Meas.*, vol. 13 (Supplement A), pp. 51–56, 1992.

[20] P. J. Liu, A. Rosell, A. Lozano, and A. Pallas-Areny, "A broadband system for multi-frequency static imaging in eit," *Clin. Phys. Physiol. Meas.*, vol. 13 (Supplement A), pp. 61–66, 1992.

[21] P. M. Record, R. G. R, and F. Vinther, "Multi-frequency eit," *Clin. Phys. Physiol. Meas.*, vol. 13 (Supplement A), pp. 67–72, 1992.

[22] J. M. Scalfe, R. C. Tozer, and I. L. Freeston, "Conductivity and permittivity images from an induced current electrical impedance tomography system," *IEE Proc. Sci. Meas. Technol.*, vol. 141, pp. 356–362, 1994.

[23] B. H. Brown, D. C. Barber, A. H. Morice, and A. D. Leathard, "Cardiac and respiratory related electrical impedance changes in the human thorax," *IEEE Transactions on Medical Engineering*, vol. 41, pp. 729–733, 1994.

[24] B. H. Brown, D. C. Barber, W. Wang, L. Lu, A. D. Leathard, R. H. Smallwood, A. R. Hampshire, R. Mackay, and K. Hatzigalanis, "Multi-frequency imaging and modelling of respiratory related electrical impedance changes," *Physiol. Meas.*, vol. 15, pp. A1–A12, 1994.

[25] J. Schlappa, E. Annese, and H. Griffiths, "Systematic errors in multy-frequency eit," *Physiol. Meas.*, vol. 21, pp. 111–118, 2000.

[26] R. J. Yerworth, R. H. Bayford, B. Brown, P. Milnes, M. Conway, and D. S. Holder, "Electrical impedance tomography spectroscopy (eits) for human head imaging," *Physiol. Meas.*, vol. 24, pp. 477–489, 2003.

[27] J. K. Seo, J. Lee, H. Zribi, S. W. Kim, and E. J. Woo, "Frequency-difference electrical impedance tomography (fdEIT): Algorithm development and feasibility study," *Physiol. Meas.*, vol. 29, pp. 929–944, 2008.

[28] S. C. Jun, J. Kuen, J. Lee, E. J. Woo, D. Holder, and J. K. Seo, "Frequency-difference eit (fdEIT) using weighted difference and equivalent homogeneous admittivity: Validation by simulation and tank experiment," *Physiological Measurement*, vol. 30, pp. 1087–1099, 2009.

[29] D. Colton and A. Kirsch, "A simple method for solving inverse scattering problems in the resonance region," *Inverse Problems*, vol. 12, pp. 383–393, 1996.

[30] A. Kirsch, "Characterization of the shape of a scattering obstacle using the spectral data of the far field operator," *Inverse Problems*, vol. 14, pp. 1489–1512, 1998.
[31] M. Brühl and M. Hanke, "Numerical implementation of two noniterative methods for locating inclusions by impedance tomography," *Inverse Problems*, vol. 16, pp. 1029–1042, 2000.
[32] M. Brühl, "Explicit characterization of inclusions in electrical impedance tomography," *SIAM J. Math. Anal.*, vol. 32, no. 6, pp. 1327–1341, 2001.
[33] M. Hanke and M. Brühl, "Recent progress in electrical impedance tomography," *Inverse Problems*, vol. 19, pp. S65–S90, 2003.
[34] M. Azzouz, M. Hanke, C. Oesterlein, and K. Schilcher, "The factorization method for electrical impedance tomography data from a new planar device," *International Journal of Biomedical Imaging*, vol. 2007, pp. Article ID 83 016, 7 pages, 2007, doi:10.1155/2007/83016.
[35] A. Kirsch and N. Grinberg, *The Factorization Method for Inverse Problems*, ser. Oxford Lecture Ser. Math. Appl. Oxford: Oxford University Press, 2007, vol. 36.
[36] B. Harrach and J. K. Seo, "Detecting inclusions in electrical impedance tomography without reference measurements," *SIAM J. Appl. Math.*, vol. 69, no. 6, pp. 1662–1681, 2009.
[37] T. I. Oh, E. J. Woo, and D. Holder, "Multi-frequency EIT system with radially symmetric architecture: KHU Mark1," *Physiol. Meas.*, vol. 28, pp. S183–S196, 2007.
[38] T. I. Oh, K. H. Lee, S. M. Kim, W. Koo, E. J. Woo, and D. Holder, "Calibration methods for a multi-channel multi-frequency EIT system," *Physiol. Meas.*, vol. 28, pp. 1175–1188, 2007.
[39] D. Isaacson, "Distinguishability of conductivities by electric current computed tomography," *IEEE Trans. Med. Imaging*, vol. 5, no. 2, pp. 91–95, 1986.
[40] B. Gebauer, "Localized potentials in electrical impedance tomography," *Inverse Probl. Imaging*, vol. 2, pp. 251–269, 2008.
[41] W. R. B. Lionheart, "EIT reconstruction algorithms: pitfalls, challenges and recent developments," *Physiol. Meas.*, vol. 25, pp. 125–142, 2004.
[42] B. Harrach and J. K. Seo, "Exact shape-reconstruction by one-step linearization in electrical impedance tomography," *accepted for publication in SIAM J. Math. Anal.*.
[43] B. Harrach, M. K. Choi and J. K. Seo, "Reducing position and shape errors in linearized EIT," *submitted to the Proceedings of the International Conference on Electrical Bioimpedance 2010*.